

Atmospheric Nitrogen Fixation via a Porous Coordination Polymer Platform with Bridging Dinitrogen Anions

Yan Xiong^{1†}, Bang Li^{1†}, Yuming Gu¹, Tong Yan¹, Zhigang Ni², Shuhua Li¹, Jing-Lin Zuo^{1*}, Jing Ma^{1*}, and Zhong Jin^{1*}

¹ State Key Laboratory of Coordination Chemistry, Key Laboratory of Mesoscopic Chemistry of MOE, Collaborative Innovation Center of Advanced Microstructures, School of Chemistry and Chemical Engineering, Nanjing University, Nanjing 210023, China.

² College of Materials, Chemistry and Chemical Engineering, Hangzhou Normal University, Hangzhou 311121, China.

*Correspondence and requests for materials should be addressed to J.-L. Zuo, J. Ma or Z. Jin (email: zuojl@nju.edu.cn; majing@nju.edu.cn; zhongjin@nju.edu.cn).

Abstract

The design of highly electron-active and stable heterogeneous catalysts for ambient nitrogen reduction reaction is challenging due to the inertness of N₂ molecule. Herein, we designed and synthesized the first zinc-based coordination polymer with bridging dinitrogen anion ligand, namely **NJUZ-1**, which is an efficient photocatalyst for atmospheric nitrogen fixation, exhibiting an outstanding ammonia conversion rate of 140 μmol g⁻¹ h⁻¹ and functioning well even with unpurified air as feeding gas. Experimental and theoretical studies revealed that the active “Zn²⁺-(N≡N)⁻¹-Zn²⁺” sites can promote the formation of NH₃, and the detachment of the yielded NH₃ creates unsaturated “Zn²⁺···Zn⁺” intermediates, which can be replenished again by external N₂ sequestration and fast intermolecular electron migration. The “Zn²⁺···Zn⁺” intermediates stabilized by the sandwiched cage-like donor-acceptor-donor framework can sustain continuous catalytic cycles via a pathway analogous to the Mars-van Krevelen process. This work presents a conceptually new strategy for nitrogen fixation via molecular active site catalysts based on metal complexes under mild conditions.

Main

The nitrogen reduction reaction (NRR) is an extremely valuable but energy-intensive chemical transformation process in which agricultural ammonia fertilizers and industrial organic nitrogen products are purposefully obtained^{1,2}. The triple bond in N₂ molecule is highly stable with a dissociation enthalpy of 941 kJ mol⁻¹³, and the lowest unoccupied molecular orbital (LUMO) (1π_g) energy of -7.91 eV is too negative to accept external electrons⁴. A classic nitrogen reduction technology in industry is the Haber-Bosch process, where high temperatures (400-500 °C) and

pressures (200-300 atm) are required to activate nitrogen by using iron-based heterogeneous catalysts⁵. Therefore, the development of more economical and environmentally-friendly nitrogen reduction methodologies has always been a grand challenge for chemists^{6,7}. Motivated by the coordination of protonated intermediates with transition metals in biological nitrogenase⁸⁻¹⁰, several representative systems have been developed¹¹⁻¹⁵. Nevertheless, for metal-dinitrogen complex systems, strong reductants must be present in excess for a continuous supply of supplying sacrificial electrons, which leads to poor cycling capability. It is critical to synthesize new catalysts that meet the following criteria: (i) possessing highly active catalytic sites for activated N₂ molecules, and (ii) exhibiting good chemical and thermal stability for recyclability.

Coordination polymers (CPs) and/or metal-organic frameworks (MOFs), have emerged as a class of molecular catalytic materials owing to their high modifiability, regular porosity, and well-defined active sites^{16,17}. When CPs act as catalysts, the uniform metal-organic scaffolds with open channels greatly facilitate the transport and diffusion of reagents and products¹⁸. Moreover, abundant catalytic sites are derived from the inherent structure of CPs, which include unsaturated metals or clusters and functional groups in the organic linkers. However, under mild conditions, metal nodes would rather be in an unsaturated state than activate inert N₂ molecules. Therefore, the CPs with dinitrogen molecules as bridging ligands have not been reported as catalysts for nitrogen fixation and direct conversion to ammonia until now.

Herein, a unique heterogeneous catalyst based on a CP with the bridging dinitrogen anion ligand $\{[\text{Zn}(\text{L})(\text{N}_2)_{0.5}(\text{TCNQ}-\text{TCNQ})_{0.5}] \cdot (\text{TCNQ})_{0.5}\}_n$ (namely **NJUZ-1**; tetra(isoquinolin-6-yl)-tetrathiafulvalene, **L**; tetracyanoquinodimethane, TCNQ) has been synthesized. The dinitrogen anions in the “Zn²⁺-(N≡N)⁻¹-Zn²⁺” sites of **NJUZ-1** can be directly converted to NH₃; the detachment of the yielded NH₃ creates an unsaturated coordinated zinc environment, that is, highly reactive “Zn²⁺...Zn⁺” intermediates, which is cycled back to “Zn²⁺-(N≡N)⁻¹-Zn²⁺” through external nitrogen sequestration and fast intermolecular electronic migration for the ensuing following catalytic cycles. This transformation sustains continuous photocatalytic cycles, and the “Zn²⁺...Zn⁺” intermediates are stabilized in the air because of the strong donor-acceptor-donor (D-A-D) cage-like sandwich structure. The observed nitrogen fixation and ammonia synthesis process in **NJUZ-1** have an analogous reaction mechanism to that of the Mars-van Krevelen (MvK) process for heterogeneous catalysis¹⁹. Density functional theory (DFT) calculations indicate that the “Zn²⁺-(N≡N)⁻¹-Zn²⁺” position was attacked and stepwisely converted to ammonia.

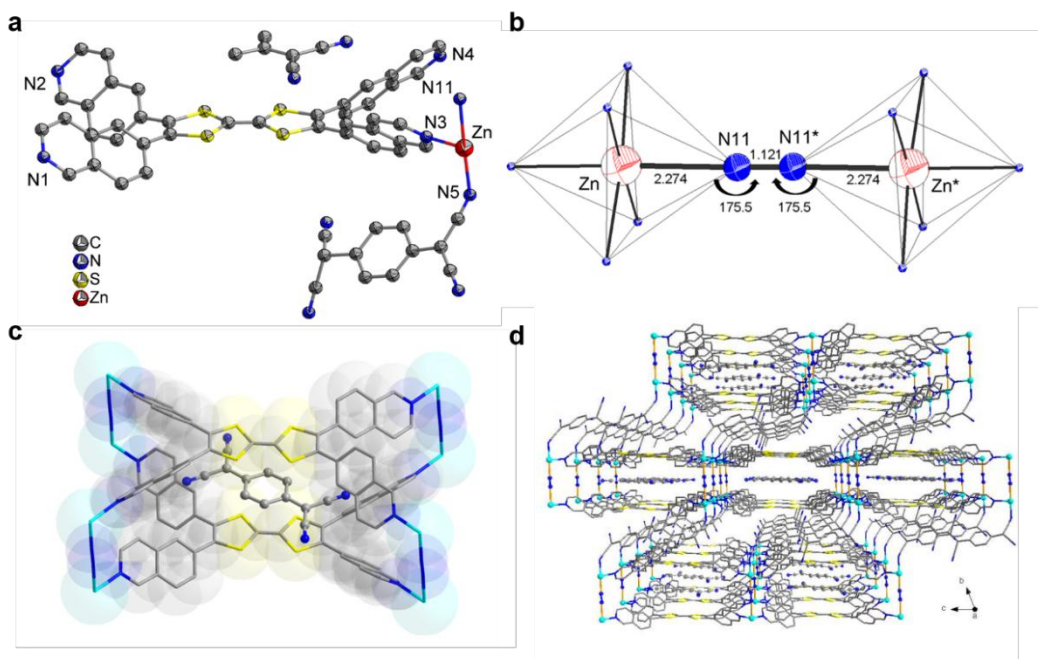


Fig. 1 Single crystal structure of **NJUZ-1**. **a** The asymmetric unit. **b** The secondary building unit (SBU) of the $[\text{Zn}_2\text{N}_2]$ asymmetric unit. Selected bond lengths and angles: Zn-N 2.274 Å, N-N 1.121 Å, N-Zn 2.274 Å, Zn-N-N 175.5°, N-N-Zn 175.5°. **c** The cage of the $[(\text{L})_2(\text{Zn}_2\text{N}_2)_4]$ structure. **d** The 3D framework with TCNQ guest molecules viewed along the a axis.

The new ligand **L** synthesized through the coupling reaction of tetrathiafulvalene (TTF) and 6-bromoisouquinoline (Extended Data Fig. 1). The **NJUZ-1**, as the first zinc-based CP with bridging dinitrogen anion ligand, was synthesized through the reaction of **L** and lithium tetracyanoquinodimethane (Li(TCNQ)) ligands with zinc nitrate at room temperature under air atmosphere. Single crystal X-ray diffraction (XRD) study reveals that **NJUZ-1** shows a (2,4,6) 3-connected three-dimensional (3D) network structure (Extended Data Fig. 2a)²⁰. Each asymmetric unit is composed of one independent Zn center, half of N_2 , one **L** ligand, half of the TCNQ-TCNQ dimer and half of the TCNQ moiety (Fig. 1a). Its secondary building units (SBUs) are pillars of $[\text{Zn}_2\text{N}_2]$ through two bilateral zinc centers and end-on dinitrogen block (Fig. 1b). Four SBUs bind with two **L** ligands to generate a molecular cage $[(\text{L})_2(\text{Zn}_2\text{N}_2)_4]$, which encapsulates a TCNQ guest molecule, and the vertical size of the TCNQ is at an optimal value (Fig. 1c). The cages of $\{(\text{L})_2[\text{Zn}_2(\text{N}_2)]_4\}$ are expanded into a 2D layered structure through SBUs in ac plane (Extended Data Fig. 2b). Afterwards, the adjacent 2D layers through the bridging of (TCNQ-TCNQ) dimer ligands to become a 3D framework (Fig. 1d).

To better understand and verify the molecular N_2 ligands of **NJUZ-1**, infrared (IR) and Raman spectroscopy analyses were performed (Extended Data Fig. 3a and b). In the IR spectrum, there are two split peaks at 2100 cm^{-1} that can be assigned to the $\text{C}\equiv\text{N}$ stretching vibration in the dimer and in the guest molecule²¹. In the Raman spectrum, a weaker peak was observed at a lower wavenumber of $\sim 2005\text{ cm}^{-1}$ that can be attributed to the instantaneous dipole moment of the symmetric dinitrogen anion,

which can be identified by the following isotope NRR experiments. The presence of this Raman peak is similar to other previously-reported dinitrogen complexes^{22,23}. Notably, the bridge-coordinated dinitrogen anion is active in the Raman analysis but inactive in the IR measurement.

Solid-state electron paramagnetic resonance (EPR) data show double splitting differential signals in the X-band frequency at room temperature (Fig. 2a), and the calculated g factor is 2.003 with typical organic unpaired radical electrons; while a relatively weak peak was detected at approximately half-field, owing to the tight coupling between the two separate single electrons²⁴. Except for the guest radical, only the dinitrogen anion, rather than the cyano groups, can offer the other vital electron, which was in good agreement with the above analysis and confirmed the existence of the dinitrogen anion. The low-temperature (93 K) and simulated EPR of **NJUZ-1** were also investigated, as shown in Extended Data Fig. 3c, which shows similar peak locations to those measured at room temperature.

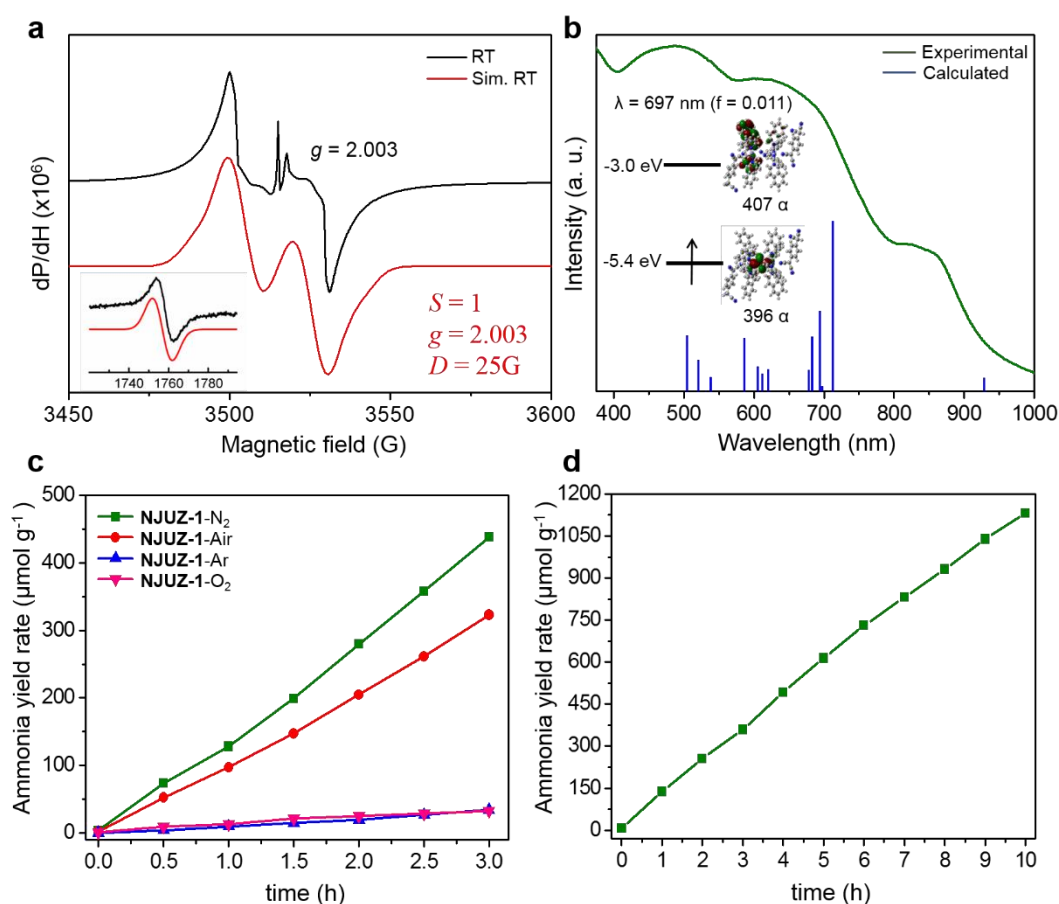


Fig. 2 Structural characterization and NRR performances of NJUZ-1. **a** Solid EPR spectrum of **NJUZ-1** measured at room temperature compared with the simulated EPR spectrum. The forbidden transitions at the half-field and simulated spectrum are shown as inserts. **b** UV-vis absorption spectrum and fingertip aspects of **NJUZ-1**. **c** Total ammonia yield rates of **NJUZ-1** in deionized water saturated by N_2 , unpurified air, Ar or O_2 flow. **d** 10 h Long-term stability test for the NRR with N_2 flow.

Remarkably, the well-defined bridging dinitrogen anion is a unique structural element of **NJUZ-1**, and the distance between nitrogen atoms is 1.121 Å (Fig. 1b and Extended Data Table 2), which is slightly longer than the length of free N≡N triple bond²⁵, indicating that the dinitrogen anion is activated. It can be observed that the as-prepared **NUJZ-1** has a lamellar nanosheet-like morphology with a diameter of approximately 100 nm, which was determined by transmission electron microscopy (TEM). The thickness quantitatively measured by atomic force microscopy (Extended Data Fig. 4a and b) was approximately 11 nm. The high porosity and ultrathin configuration of these nanosheets leads to good nitrogen adsorption capability at room temperature (Extended Data Fig. 4c), bringing a large number of open channels and reactive sites. Meanwhile, the diffuse reflectance spectroscopy reveal that the **NJUZ-1** has strong light absorption capability at ultraviolet and visible regions (Fig. 2b), which is attributed to the metal-to-ligand charge transfer (MLCT) or intramolecular charge transfer between TTF and TCNQ molecules as verified by time-dependent density functional theory (TDDFT) calculation (Extended Data Fig. 5), indicating its good photo-response properties. All these advantageous structural features and physiochemical properties of **NJUZ-1** hold tremendous possibility for photocatalytic nitrogen fixation.

The photo-reduction performances of **NJUZ-1** for the NRR were investigated in deionized water with a typical cylindrical quartz reactor under light irradiation of a 300 W Xe lamp without cut-off filter. The yield of ammonia was detected by ion chromatography. Fig. 2c shows that the ammonia produced by the **NJUZ-1** photocatalyst with purified N₂ flow as feeding gas is measured to be 140 μmol g⁻¹ h⁻¹, which is competitive among the state-of-the-art photocatalysts²⁶. Notably, no hydrazine by-product was detected after the photocatalytic NRR process. Besides, no product was generated in the dark. To broaden the practical application range in photocatalytic NRR, unpurified air flow was also tested as alternative feeding gas. As shown in Fig. 2c, we notice that the photocatalytic activity of **NJUZ-1** with air flow remains high, showing an average ammonia yield rate of 102.40 μmol g⁻¹ h⁻¹ in air, which is approximately 73% of the activity in pure N₂ (Extended Data Fig. 6a). This percentage value is slightly lower than the mole percentage of N₂ in ambient atmosphere, which could be ascribed to the lower solubility of N₂ in water. This result indicates that the **NJUZ-1** photocatalyst has an extraordinary tolerance towards ambient atmosphere, indicating its great potential for large-scale and economical nitrogen fixation applications in industry. The long-term catalytic stability of **NJUZ-1** has also been examined, as shown in Fig. 2d and Extended Data Fig. 6b. During the long-term photocatalytic test for 10 h or 25 h, the NRR performance was well maintained and the concentration of yielded ammonia increased almost linearly along with the reaction time. This result confirms the high stability of **NJUZ-1** during the long-term photocatalytic process. In addition, XRD and TEM characterizations (Extended Data Fig. 6c-e) show that the crystalline structure and morphology of **NJUZ-1** remain almost unchanged without structural degradation after long-term photocatalytic testing, further confirming the well-preserved structural integrity and high stability. To investigate the possible N sources of the produced ammonia, Ar or

O₂ flow were also employed as feeding gases in the control experiments. As shown in Fig. 2c, when Ar or O₂ was used as the feeding gas, only a trace amount of ammonia was generated as the time of light irradiation increased, which is originated from the dinitrogen anions that are already bonded in the “Zn²⁺-(N≡N)⁻¹-Zn²⁺” sites. These results preliminarily verify that the NJUZ-1 photocatalyst can not only convert the dinitrogen species contained in its own lattice to ammonia, but also can rapidly convert the external N₂ source to ammonia.

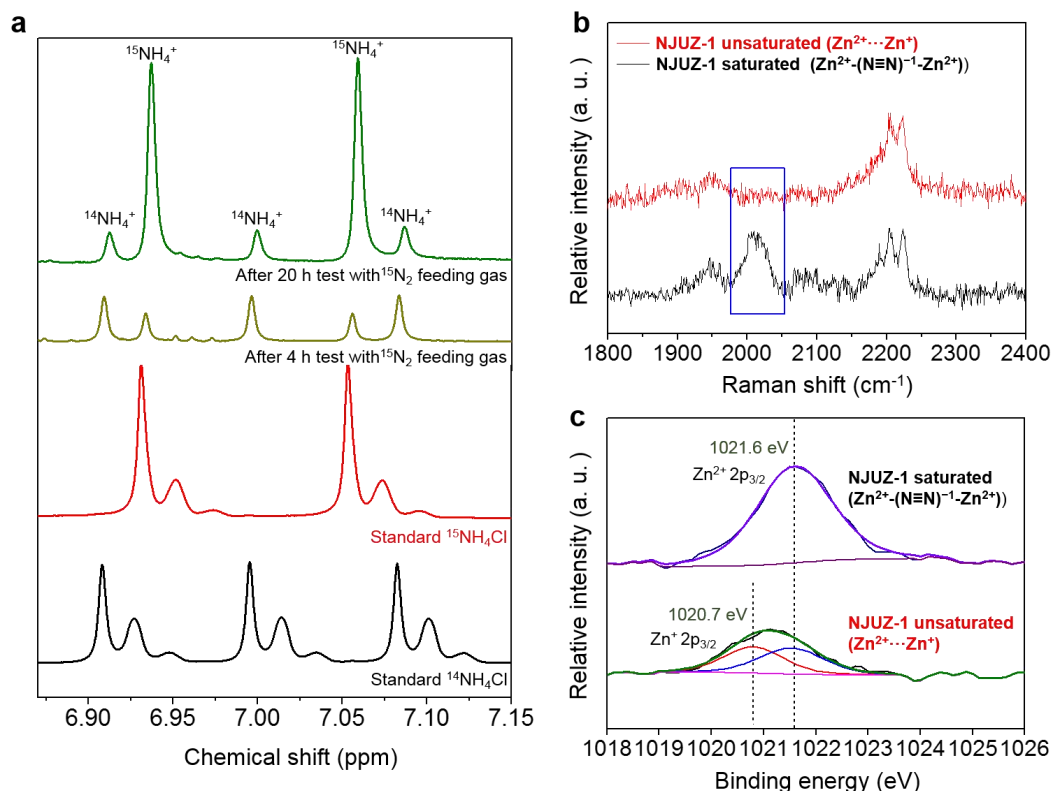


Fig. 3 **a** ¹H NMR spectra of the standard ¹⁴NH₄Cl, ¹⁵NH₄Cl samples and the products yielded with ¹⁵N₂ feeding gas after different test times. **b** Raman spectra of NJUZ-1 measured at pristine state (saturated) and after the NRR process (unsaturated). **c** XPS spectra of NJUZ-1 measured at pristine state (saturated) and after the NRR process (unsaturated).

To gain further insight into the involvement of the “Zn²⁺-(N≡N)⁻¹-Zn²⁺” sites in NJUZ-1 for the photocatalytic NRR, ¹⁵N₂ was employed as the feeding gas to identify the occurrence of dinitrogen replacement with the aid of ¹H nuclear magnetic resonance (¹H-NMR) measurements. Fig. 3a shows the ¹H NMR spectra of standard ¹⁴NH₄Cl, ¹⁵NH₄Cl samples and the photocatalytic product yielded with the ¹⁵N₂ feeding gas after 4 h and 20 h of reaction time. As expected, the presence of both ¹⁴NH₄⁺ and ¹⁵NH₄⁺ was detected in the ¹H NMR spectra after the photocatalytic reaction process of 4 and 20 h. The ¹⁵NH₄⁺ peaks are located at the chemical shifts around 6.94 and 7.06, respectively; and the ratio of the collective integral area of the ¹⁵NH₄⁺ peaks after 4 and 20 h of reaction time is 9.81, indicating continuous ¹⁵NH₄⁺ production. In contrast, the ¹⁴NH₄⁺ peaks are centered around the chemical shifts of 6.91, 7.00 and 7.09; and the ratio of the collective integral area of the ¹⁴NH₄⁺ peaks

after 4 h and 20 h of reaction time is 1.08, indicating that the production of $^{14}\text{NH}_4^+$ was terminated owing to the complete depletion of the initial ^{14}N source in the reaction system (such as the dissolved $^{14}\text{N}_2$ in water and the dinitrogen species in the lattice of **NJUZ-1**). The isotopic labelling experiment reveals that the significantly increased content of $^{15}\text{NH}_4^+$ product is derived from the photocatalytic NRR process with the external $^{15}\text{N}_2$ feeding gas as raw material.

To investigate the possible reaction intermediates during the photocatalytic process, Raman spectroscopy and X-ray photoelectron spectroscopy (XPS) were performed on **NJUZ-1** at the pristine state and after the NRR. The Raman spectrum of pristine **NJUZ-1** shows a broad peak between 1980 to 2050 cm^{-1} (Fig. 3b), which is originated from the saturated “ $\text{Zn}^{2+}-(\text{N}\equiv\text{N})^{-1}-\text{Zn}^{2+}$ ” sites. However, after the reaction was suspended, this peak became weaker and finally disappeared, which indicates the disappearance of the dinitrogen anions. The Zn $2\text{P}_{3/2}$ XPS spectrum of pristine **NJUZ-1** (Fig. 3c) only shows a peak located around 1021.6 eV, confirming the presence of Zn^{2+} species²⁷. However, after the NRR process, this peak became weaker and another peak located at 1020.7 eV with the comparable intensity was appeared, indicating that half of the Zn^{2+} species were converted to Zn^+ species. Meanwhile, in the $^{15}\text{N}_2$ isotopic labelling experiment, the solid-state NMR spectrum of **NJUZ-1** after the reaction of $^{15}\text{N}_2$ and water shows no characteristic peak of ^{15}N (Fig. 3b and Extended Data Fig. 6f), indicating the absence of $(^{15}\text{N}\equiv^{15}\text{N})^{-1}$ anions and the unsaturated state of **NJUZ-1** with the form of “ $\text{Zn}^{2+}\cdots\text{Zn}^+$ ” intermediates. All these results indicate that the saturated “ $\text{Zn}^{2+}-(\text{N}\equiv\text{N})^{-1}-\text{Zn}^{2+}$ ” sites are transformed to unsaturated “ $\text{Zn}^{2+}\cdots\text{Zn}^+$ ” intermediates during the NRR process.

Consequently, a reasonable hypothesis was proposed that the unsaturated “ $\text{Zn}^{2+}\cdots\text{Zn}^+$ ” intermediates were formed during photocatalytic NRR process, and the photocatalyst can be regenerated repeatedly by external dinitrogen exchange cycles which is analogous to the MvK process¹⁹, as illustrated in Fig. 4a. The unsaturated zinc nodes without dinitrogen anions were situated in the cage-like structure through $\pi\cdots\pi$ interactions and hydrogen bonds, where the TCNQ guest located at the center of the cage plays a vital role to serve as a counterion and also stabilize the crystal structure. The crystal structure of **NJUZ-1** undergoes an almost non-destructive dinitrogen intercalation and deintercalation process, and the powder XRD (PXRD) patterns and UV-vis spectra remain nearly unchanged. Notably, TTF-TCNQ is a well-known organic D-A-type conductor, while the distance between TTF and TCNQ is approximately 3.473 and 3.168 Å, respectively²⁸⁻³⁰. Spatially consecutive D-A-D cage-like sandwich structures provided an excellent platform to sustain the catalytic cycles, while the lower valence and unsaturated metal (Zn^+ species) offered the necessary electrons to activate nitrogen, which are two indispensable factors for the photocatalytic nitrogen fixation and conversion system of **NJUZ-1** (Fig. 4a).

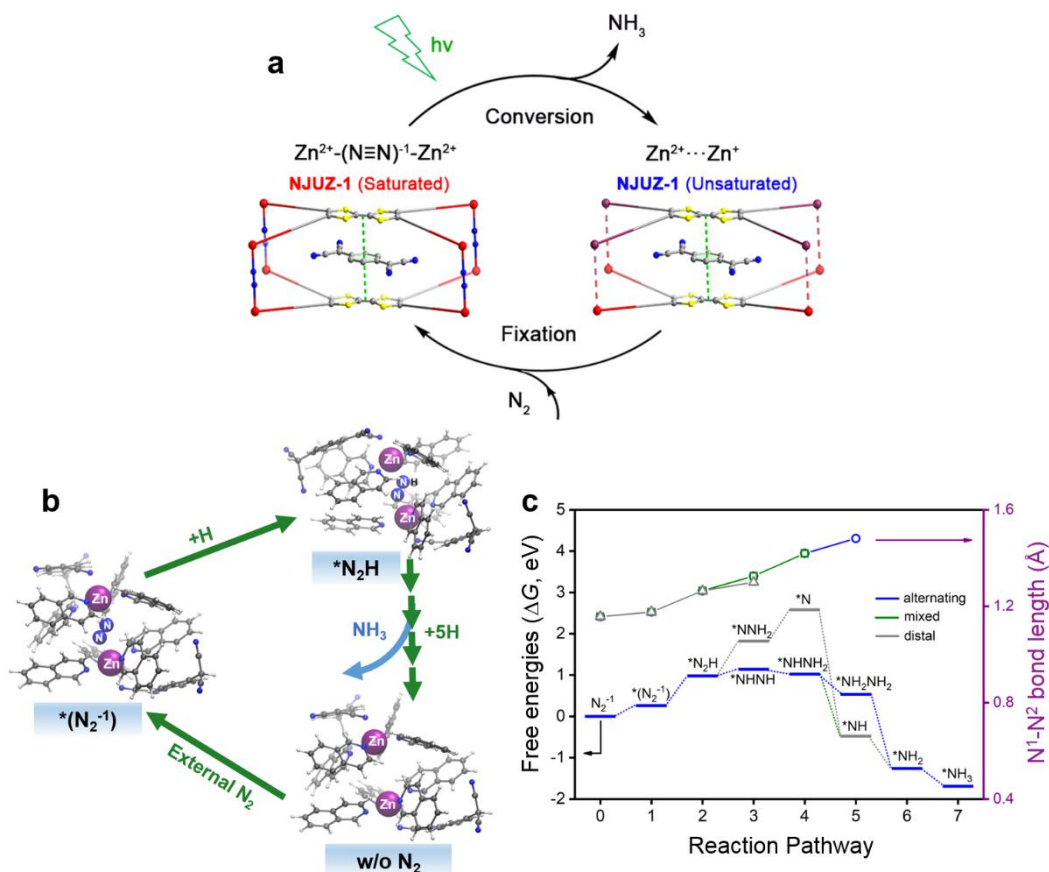


Fig. 4 **a** Scheme cycling mechanism of **NJUZ-1** during photocatalytic NRR process. **b** The schematic illustration of possible reaction pathway for NRR process over **NJUZ-1**. **c** The variation of the calculated free energies and N-N bond lengths in each step of different possible pathways.

TTF-TCNQ (D-A-type) species, as the charge-transfer light absorbers, significantly contribute to the functions of absorbing light energy and facilitating the separation of electrons and holes. The absorption peak of **NJUZ-1** calculated by TDDFT method is located at 716 nm in the visible light region (Extended Data Fig. 5) and is assigned as the intramolecular photo-generated charge transfer between TTF and TCNQ. As shown in Extended Data Fig. 5d, the related singly occupied orbitals are mainly localized on TTF and TCNQ, respectively. The photo-excited electrons are then transmitted to the “ $\text{Zn}^{2+}-(\text{N}\equiv\text{N})^{-1}-\text{Zn}^{2+}$ ” sites to activate the dinitrogen anions, corresponding to the S_1 state (Extended Data Fig. 7ab). The first hydrogenation step is triggered by a proton and coupled with an electron attacking to form the N_2H^* intermediates (Fig. 4b and Extended Data Fig. 7bc). In this step, the free energy uphill barrier is predicted to be 0.72 eV using a periodic boundary condition (PBC) model in the ground state (S_0). Compared with the S_0 state, the hydrogenation step in the S_1 excited state is thermodynamically more favourable, which is an exothermic process. Then, three possible reaction pathways, including the alternating (blue), distal (grey) and mixed (green) pathways^{31,32}, are displayed in Extended Data Fig. 7bc. Among them, the alternating pathway is more favourable for the NRR via **NJUZ-1**. Subsequently, another proton attacks the other N atom to form the NHNH^* species, with an increase around 0.16 eV in free energy. During the following possible hydrogenation steps, including the reduction of NHNH^* to NHNH_2^* , NHNH_2^* to

NH_2NH_2^* , and NH_2NH_2^* to the release of the first NH_3 , the free energy decreases by -0.12 , -0.49 , and -1.79 eV in PBC at PBE-D3 level, respectively. Meanwhile, the $\text{N}_1\text{-N}_2$ bond length is gradually increased during these dinitrogen activation steps, as shown in Fig. 4c. Finally, the formation of the second NH_3 has a decrease in free energy of -0.43 eV. The catalytic cycle is completed after the release of the second NH_3 , where the change of free energy is calculated to be -0.34 eV. We also investigated Mulliken charge variations in each elementary step (Extended Data Fig. 7d). The inspection on the Mulliken charge reveals that the charge value on Zn atoms (1.68 e) in saturated ($\text{Zn}^{2+}\text{-(N}_2\text{)}^{-1}\text{-Zn}^{2+}$) moieties is smaller than those unsaturated ($\text{Zn}^{2+}\text{-(N}_2\text{)}^{-1}\text{-Zn}^{2+}$) moieties (1.70 e) in PBC model. It demonstrates that the N_2 molecule gains 0.20 e from **NJUZ-1**, which increases the length of $\text{N}\equiv\text{N}$ bond. The electron transfer mainly occurs between N_{2-m}H_n species and the framework, where **NJUZ-1** can serve as an electron reservoir during the NRR process.

The PBE-D3 results were further validated by using six different theoretical levels, including the choice of different basis sets and DFT functionals (Extended Data Tables 4-7; Extended Data Fig. 8) as well as the DLPNO-CCSD(T)-based wave function methods (Extended Data Table 8), with the cluster model containing $\text{Zn}^{2+}\text{-(N}\equiv\text{N)}^{-1}\text{-Zn}^{2+}$ catalytic site. The relative energies to the lowest energy species are close to each other under different theoretical levels with deviations less than 0.2 eV. The different level computations also displayed the similar trends in the free energy changes, ΔG , of endothermic processes in nitrogen reduction reaction and spin preference, indicating insensitivity of the computed values to the choice of functionals and basis sets provided that the computational level is high enough.

In summary, we demonstrate that the zinc-based coordination polymer with the bridging dinitrogen anion ligand can efficiently realize photocatalytic nitrogen fixation and conversion in ambient environment without the need of external electron-sacrificial reagent. The highly reactive bridge-coordinated “ $\text{Zn}^{2+}\text{-(N}\equiv\text{N)}^{-1}\text{-Zn}^{2+}$ ” sites in the well-defined **NJUZ-1** framework was repeatedly and reversibly converted to the “ $\text{Zn}^{2+}\cdots\text{Zn}^{2+}$ ” intermediates during the NRR process. The crucial features presented in the inherent molecular structure of **NJUZ-1** for photocatalytic NRR are: (i) the unsaturated and variable-valence metal cores offer the necessary vacant sites and transmit the excited electrons to activate dinitrogen species; (ii) the D-A-D cage structure provides a stable platform for light harvesting and sustaining the catalytic cycles. We believe that this work provides the direct evidence for understanding the mechanism on nitrogen fixation and conversion at molecular level, and broaden the choices on model catalysts based on metal complexes for efficient and stable artificial nitrogen activation and application.

References

1. G. Ertl, Reactions at Surfaces: From Atoms to Complexity (Nobel Lecture). *Angew. Chem. Int. Ed.* **47**, 3524-3535 (2008).
2. S. L. Foster, S. I. P. Bakovic, R. D. Duda, S. Maheshwari, R. D. Milton, S. D. Minter, M. J. Janik, J. N. Renner, L. F. Greenlee, Catalysts for nitrogen reduction to ammonia. *Nat. Catal.* **1**, 490-500 (2018).
3. H.-P. Jia, E. A. Quadrelli, Mechanistic aspects of dinitrogen cleavage and hydrogenation to produce ammonia in catalysis and organometallic chemistry: relevance of metal hydride bonds and dihydrogen. *Chem. Soc. Rev.* **43**, 547-564

- (2014).
4. A. Hinchliffe, *Chemical Modelling: Applications and Theory*, Volume 5 (RSC publishing, 2009).
 5. T. Rayment, R. Schlögl, J. M. Thomas, G. Ertl, Structure of the ammonia synthesis catalyst. *Nature* **315**, 311-313 (1985).
 6. F. Zhou, L. M. Azofra, M. Ali, M. Kar, A. N. Simonov, C. McDonnell-Worth, C. Sun, X. Zhang, D. R. MacFarlane, Electro-synthesis of ammonia from nitrogen at ambient temperature and pressure in ionic liquids. *Energy Environ. Sci.* **10**, 2516-2520 (2017).
 7. K. Ithisuphalap, H. Zhang, L. Guo, Q. Yang, H. Yang, G. Wu, Photocatalysis and photoelectrocatalysis methods of nitrogen reduction for sustainable ammonia synthesis. *Small Methods* **3**, 1800352 (2019).
 8. B. A. MacKay, M. D. Fryzuk, Dinitrogen coordination chemistry: on the biomimetic borderlands. *Chem. Rev.* **104**, 385-402 (2004).
 9. B. M. Hoffman, D. Lukoyanov, Z.-Y. Yang, D. R. Dean, L. C. Seefeldt, Mechanism of nitrogen fixation by nitrogenase: the next stage. *Chem. Rev.* **114**, 4041-4062 (2014).
 10. Y. Zhang, J.-L. Zuo, H.-C. Zhou, R. H. Holm, Rearrangement of symmetrical dicubane clusters into topological analogues of the P cluster of nitrogenase: nature's choice? *J. Am. Chem. Soc.* **124**, 14292-14293 (2002).
 11. D. V. Yandulov, R. R. Schrock, Catalytic reduction of dinitrogen to ammonia at a single molybdenum center. *Science* **301**, 76-78 (2003).
 12. K. Arashiba, Y. Miyake, Y. Nishibayashi, A molybdenum complex bearing PNP-type pincer ligands leads to the catalytic reduction of dinitrogen into ammonia. *Nat. Chem.* **3**, 120-125 (2011).
 13. J. S. Anderson, J. Rittle, J. C. Peters, Catalytic conversion of nitrogen to ammonia by an iron model complex. *Nature* **501**, 84-87 (2013).
 14. M. J. Chalkley, M. W. Drover, J. C. Peters, Catalytic N₂-to-NH₃ (or -N₂H₄) conversion by well-defined molecular coordination complexes. *Chem. Rev.* **120**, 5582-5636 (2020).
 15. Y. Roux, C. Duboc, M. Gennari, Molecular Catalysts for N₂ Reduction: State of the Art, Mechanism, and Challenges. *Chem. Phys. Chem.* **18**, 2606-2617(2017).
 16. Q. Yang, Q. Xu, H.-L. Jiang, Metal-organic frameworks meet metal nanoparticles: synergistic effect for enhanced catalysis. *Chem. Soc. Rev.* **46**, 4774-4808 (2017).
 17. H.-Y. Wang, L. Cui, J.-Z. Xie, C. F. Leong, D. M. D'Alessandro, J.-L. Zuo, Functional coordination polymers based on redox-active tetrathiafulvalene and its derivatives. *Coord. Chem. Rev.* **345**, 342-361 (2017).
 18. L. Jiao, Y. Wang, H.-L. Jiang, Q. Xu, Metal-Organic Frameworks as platforms for catalytic applications. *Adv. Mater.* **30**, 1703663 (2018).
 19. P. Mars, D. W. van Krevelen, Oxidations carried out by means of vanadium oxide catalysts. *Chem. Eng. Sci.* **3**, 41-59 (1954).
 20. V. A. Blatov, A. P. Shevchenko, D. M. Proserpio, Applied topological analysis of crystal structures with the program package ToposPro. *Cryst. Growth Des.* **14**, 3576-3586 (2014).

21. J. Kim, A. Silakov, H. P. Yennawar, B. J. Lear, Structural, electronic, and magnetic characterization of a dinuclear Zinc complex containing TCNQ⁻ and a μ -[TCNQ-TCNQ]₂⁻ ligand. *Inorg. Chem.* **54**, 6072-6074 (2015).
22. S. E. Creutz, J. C. Peters, Diiron bridged-thiolate complexes that bind N₂ at the Fe^{II}Fe^{II}, Fe^{II}Fe^I, and Fe^IFe^I redox states. *J. Am. Chem. Soc.* **137**, 7310-7313 (2015).
23. M. A. Nesbit, P. H. Oyala, J. C. Peters, Characterization of the earliest intermediate of Fe-N₂ protonation: CW and pulse EPR detection of an Fe-NNH species and its evolution to Fe-NNH₂⁺. *J. Am. Chem. Soc.* **141**, 8116-8127 (2019).
24. N. M. Gallagher, J. J. Bauer, M. Pink, S. Rajca, A. Rajca, High-spin organic diradical with robust stability. *J. Am. Chem. Soc.* **138**, 9377-9380 (2016).
25. A. Wilson, Tables of interatomic distances and configuration in molecules and ions. *Acta Cryst.* **12**, 174 (1959).
26. M. Li, H. Huang, J. Low, C. Gao, R. Long, Y. Xiong, Recent progress on electrocatalyst and photocatalyst design for nitrogen reduction. *Small Methods* **3**, 1800388 (2019).
27. P. Cui, H.-S. Hu, B. Zhao, J. T. Miller, P. Cheng, J. Li, A multicentre-bonded [ZnI]₈ cluster with cubic aromaticity. *Nat. Commun.* **6**, 6331 (2015).
28. T. C. Narayan, T. Miyakai, S. Seki, M. Dincă, High charge mobility in a tetrathiafulvalene-based microporous Metal-Organic Framework. *J. Am. Chem. Soc.* **134**, 12932-12935 (2012).
29. J. Su, W. He, X.-M. Li, L. Sun, H.-Y. Wang, Y.-Q. Lan, M. Ding, J.-L. Zuo, High electrical conductivity in a 2D MOF with intrinsic superprotonic conduction and interfacial pseudo-capacitance. *Matter* **2**, 711-722 (2020).
30. H. Alves, A. S. Molinari, H. Xie, A. F. Morpurgo, Metallic conduction at organic charge-transfer interfaces. *Nat. Mater.* **7**, 574-580 (2008).
31. S. M. Bhutto, P. L. Holland, Dinitrogen Activation and Functionalization Using β -Diketiminato Iron Complexes. *Eur. J. Inorg. Chem.* 1861-1869 (2019).
32. S. L. Foster¹, S. I. P. Bakovic, R. D. Duda, S. Maheshwari, R. D. Milton, S. D. Minter, M. J. Janik, J. N. Renner, L. F. Greenlee, Catalysts for nitrogen reduction to ammonia. *Nat, Catal.* **1**, 490-500 (2018).

Methods

Chemicals

The starting materials were of analytical grade and were used as commercially obtained without further purification.

Synthesis of the **L** ligand

[Tetra(isoquinolin-6-yl)-tetrathiafulvalene] (**L**) was prepared by a reflux reaction process, as illustrated in Extended Data Fig. 1. Briefly, Pd(OAc)₂ (84 mg), P(*t*-Bu₃)·HBF₄ (320 mg) and Cs₂CO₃ (240 mg) were placed in a 50 mL 1,4-dioxane reaction flask under N₂ atmosphere. A mixture of tetrathiafulvalene (300 mg) and 6-bromoisoquinoline (1.8 g) was added³⁰. The reacted mixture was refluxed for 48 h. The organic compounds were extracted with chloroform for three times. The organic compounds were purified by column chromatography with silica gel using petrol ether-dichloromethane as fluid phase to afford target product **L** as a dark green solid powder (yield: 73%). ¹HNMR (CDCl₃): δ = 9.21 (4H), δ = 8.54 (4H), δ = 7.86 (4H), δ = 7.81 (4H), δ = 7.58 (4H), δ = 7.35 (4H).

Synthesis of Li(TCNQ)

Briefly, tetracyanoquinodimethane (TCNQ, 6.7 g) and LiI (13.4 g) were placed in dry boiling acetonitrile under N₂ atmosphere. The mixture was stirred for 1 h and cooled to room temperature. The light-precipitated purple solid (5.9 g) was washed and filtered with acetonitrile and diethyl ether for several times. Then, the product was dried under vacuum overnight.

Synthesis of NJUZ-1

NJUZ-1 was prepared based on **L** and Li(TCNQ). A solution of Zn(NO₃)₂ (0.04 mmol) in CH₃OH was allowed to diffuse into the solution of **L** (0.01 mmol) and freshly prepared Li(TCNQ) (0.02 mmol) in CHCl₃ and DMF at atmospheric pressure and room temperature, leaving several shining dark crystals suitable for XRD analysis after kept approximately 1 week on the wall of test tube. Yield: 57% based on **L**. Elemental analysis of **NJUZ-1**, theoretical: C 60.10%, N 12.64%, H 2.55%; Found: C 58.43%, N 11.42%, H 3.04%. Unless specified otherwise, this synthesis method was also used to prepare bulk samples for the following characterizations and photocatalysis experiments. The isotope labelled ¹⁵N-**NJUZ-1** was synthesized similarly to **NJUZ-1**, except that all steps are borrowed from Schlenk technology under ¹⁵N₂ environment. The diffusion was left for two weeks at room temperature, and dark red crystals were obtained. Yield: 32% based on **L**.

Structural analysis of NJUZ-1 single crystals

Single crystal X-ray diffraction (XRD) study reveals that each asymmetric unit of **NJUZ-1** contains one independent Zn center, half of N₂, one **L** ligand, half of the TCNQ-TCNQ dimer, and half of the TCNQ moiety (Fig. 1a). As shown in Fig. 1b, the central Zn(II) ion adopts a distorted octahedral coordination environment, which is defined by four nitrogen donors from four **L** ligands in the equatorial plane and two

nitrogen donors from dinitrogen and the TCNQ-TCNQ dimer. In cage of $[(\mathbf{L})_2(\text{Zn}_2\text{N}_2)_4]$, the TCNQ core is sandwiched between the TTF roof and floor units with an average $\pi \cdots \pi$ stacking distance of 3.652 Å, while the hydrogen atoms on the eight isoquinoline groups point towards the N atoms of TCNQ with C-H \cdots N distances ranging from 2.667 to 3.022 Å (Extended Data Fig. 2c). It is worth noting that TCNQ acts as a μ -dimer and a single radical molecule in the **NJUZ-1** crystal lattice. One of the most important features in TCNQ species is that the different bond lengths will take on different charge states, and the charge on each TCNQ can be calculated using Kistenmacher's empirical formula²⁰. These values (Extended Data Table 3) are close to the expected charges of -1 and -2 for the TCNQ and (TCNQ-TCNQ) dimers, respectively. The central C=C bond length of the TTF core is 1.323 Å (Extended Data Table 2), suggesting that the TTF moiety is in a neutral state³¹. The scarcity of other supplementary charged species in the crystal channel confirmed the distribution of the valences in the asymmetric unit. In brief, one positive divalent Zn^{2+} ion completely corresponds to half of a negative divalent bridging dimer, half of a guest radical and half of an unidentified dinitrogen anion.

Characterizations

The C, H and N microanalyses were carried out with a Vario Micro Cube elemental analyser. For Fourier transform infrared (FT-IR) spectroscopy measurements, the samples were prepared into KBr pellets and the FT-IR spectra were recorded in the range of 4000-400 cm^{-1} on a Vector22 Bruker spectrophotometer. Raman spectra were obtained with a LabRAM Aramis with a 633 nm laser wavelength. UV-vis diffuse reflectance spectroscopy (DRS) were performed with a Shimadzu UV-2600 instrument using BaSO_4 powder as the reference sample. TEM (JEM-4800) was used for the morphological and structural characterizations. Topographic AFM characterizations were performed using a Bruker Dimension Icon instrument. A ScanAsyst model and RTESP probe were used to measure the morphology and thickness of the **NJUZ-1** nanosheets. PXRD patterns were obtained at room temperature on a Bruker D8 ADVANCE instrument (Cu $\text{K}\alpha_1$, $\lambda = 1.54056$ Å; $\text{K}\alpha_2$, $\lambda = 1.54439$ Å) at a rate of 0.1°/s. XPS measurements were performed by a PHI-5000 Versa Probe instrument equipped with an Al $\text{K}\alpha$ monochromatized X-ray radiation source. The room-temperature EPR spectra were analysed by a Bruker ER-420 spectrometer with a 9.4452 GHz modulating magnetic field in the X band. Nitrogen adsorption measurements were performed on a Quantachrome Autosorb-IQ-2CTCD-VP instrument at room temperature.

Single crystal data were collected on a Bruker D8 Venture Photon II instrument (Ga $\text{K}\alpha$ radiation, $\lambda = 0.71073$ Å) at 223(2) K and reduced with APEX3 software. The absorption corrections were applied using SADABS method. The crystal structures were solved and refined against F^2 by the full-matrix least-squares using the SHELXL-2016/6 programs. The positions of the metal atoms and their first coordination spheres were located from direct method E-maps. All non-hydrogen atoms were refined with anisotropic thermal parameters, and hydrogen atoms were calculated theoretically, placed onto specific atoms and refined isotopically with fixed

thermal factors. Free solvent molecules of CHCl_3 were removed from the data set using the SQUEEZE routine of PLATON and refined further using the generated data.

CCDC 2008863 contain the supplementary crystallographic data for this paper. These data can be obtained free of charge via www.ccdc.cam.ac.uk/data_request/cif, or by emailing data_request@ccdc.cam.ac.uk, or by contacting The Cambridge Crystallographic Data Centre, 12 Union Road, Cambridge CB2 1EZ, UK; fax: +44 1223 336033.

Computational methods

1. Computational details and the choice of theoretical levels

Density functional theory (DFT) calculations in periodic boundary condition (PBC) model were performed by using the Cambridge Serial Total Energy Package (CASTEP) module in the Materials Studio software package³². The generalized gradient approximation (GGA) method together with the Perdew-Burke-Ernzerhof (PBE) as the exchange-correlation functional³³, and the ultrasoft pseudopotential were employed in both geometry optimizations and electronic property calculations. The Grimme method was applied to take the van der Waals interactions into account^{34,35}. The PBC model with a cell size of $12.4 \times 16.3 \times 38.9 \text{ \AA}^3$, was employed to model the systems of NJUZ-1. The energy cut-off of 450 eV was employed in our calculations. The Brillouin zone (BZ) was sampled with a $1 \times 1 \times 1$ k-point for geometry optimization. The energy convergence value between two consecutive steps was chosen as 2×10^{-5} eV, and a maximum force was allowed lower than 0.05 eV/Å on each atom.

The Gibbs free energy change (ΔG) of the intermediates in the NRR was calculated by employing the computational hydrogen electrode (CHE) model, which uses one-half of the chemical potential of hydrogen as the chemical potential of the proton-electron pair³⁶. The value of ΔG between two steps involved in the NRR process can be expressed as:

$$\Delta G = G(\text{N}_{2-m}\text{H}_n@\text{NJUZ-1}) + m G(\text{NH}_3) - G(\text{N}_2) - n/2 G(\text{H}_2) - G(\text{NJUZ-1})$$

where $G(\text{N}_{2-m}\text{H}_n@\text{NJUZ-1})$ is the Gibbs free energy of the intermediates in NJUZ-1. $G(\text{NH}_3)$, $G(\text{N}_2)$, $G(\text{H}_2)$, and $G(\text{NJUZ-1})$ are the Gibbs free energy values of ammonia, dinitrogen, hydrogen, and the substrate, respectively; n is the number of H^+/e^- pairs transferred; and m ($m = 0, 1$) is the number of NH_3 molecules released. The computational results of DFT/PBE-PBC are presented in Extended Data Fig. 7 and Extended Data Table 6.

To gain the insight into the reaction pathway of nitrogen reduction reaction, the cluster model containing $\text{Zn}^{2+}-(\text{N}\equiv\text{N})^{-1}-\text{Zn}^{2+}$ as catalytic site was built from the crystal structure, as shown in Extended Data Fig. 8. The reaction steps of endothermic process were calculated by different functionals and basis sets in the Gaussian 16 package suite³⁷. The geometry optimizations and frequencies of intermediates were carried out at **six different theoretical levels**, including **level1**: B3LYP-D3 with a mixed basis set combination (def2-SVP³⁸ basis set on C, N, and H atoms, LANL2DZ basis set on Zn atoms, in a polarizable continuum solvent model, CPCM³⁹, and D3BJ

empirical dispersion); **level2**: BP86-D3^{40,41} with a mixed basis set combination (def2-SVP basis set on C, N, and H atoms, SDD basis set on Zn atoms, in a polarizable continuum solvent model, CPCM, and D3BJ empirical dispersion); and **level3**: M06-L-D3⁴² with a mixed basis set combination (def2-SVP basis set on C, N, and H atoms, SDD basis set on Zn atoms, in a polarizable continuum solvent model, CPCM, and D3 empirical dispersion). Then, the high-level single point energy computations were employed, including basis set **level4**: def2-TZVPP⁴³ basis set on C, N, and H atoms, SDD basis set on Zn atoms in a polarizable continuum solvent model, CPCM, and D3BJ empirical dispersion; **level5**: def2-TZVP basis set; **level6**: def2-TZVPP basis set. The **level1-level4** computation results are presented in Extended Data Table 4 (the number of basis functions); Extended Data Table 5 (the energy and relative energy of intermediates); Extended Data Table 6 (the free energy change along reaction path); Extended Data Table 7 (the spin preference of intermediates).

2. Time-dependent density functional theory (TDDFT) calculations of excitation energies

Time-dependent density functional theory (TDDFT) calculations of the excitation energies were performed with the Gaussian 16 package suite³⁷. Geometry optimizations were carried out by using DFT with the B3LYP functional. The 6-31G(d) basis set was employed for C, H, N, and S atoms, while the LANL2DZ basis set, together with the related effective core potentials, was used for Zn atoms. The calculations of the vertical excitation energies of ligands or **NJUZ-1** units were performed at the optimized geometries in the ground states (S_0). The TDDFT optimized geometries of the first excited singlet (S_1) states were also obtained. The computational results are presented in Extended Data Fig. 5.

To reveal important fingertip aspects in UV-vis spectra of **NJUZ-1** (Extended Data Fig. 5a), two clusters were chosen to study the electronic structure of the low-lying excited states as shown in Extended Data Fig. 5b. For the **clusterA** ($N_{\text{basis}} = 1764$), including $\text{Zn}^{2+}-(\text{N}_2)^{-1}-\text{Zn}^{2+}$ moiety, quinoline, and TCNQ ligands, the absorption peaks calculated by TDDFT method located at 589, 686, 697 and 931 nm could be attributed to the metal-to-ligand charge transfer (MLCT), as shown in Extended Data Fig. 5c. The related 396α orbital is mainly localized on the $\text{Zn}^{2+}-(\text{N}_2)^{-1}-\text{Zn}^{2+}$ moiety, and 412α , 408α , 407α , and 404α orbitals are mainly attributed to the quinoline ligands in **clusterA**. The absorption peak of **clusterB** (TCNQ-TTF-TCNQ, $N_{\text{basis}} = 1876$) is located at 716 nm in the visible light region, as shown in Extended Data Fig. 5d, which is assigned as the intramolecular charge transfer between TTF and TCNQ molecules. The related 418β and 421β orbitals are mainly localized on TTF and TCNQ molecules, respectively. The absorption peak at 508 nm could be ascribed to the intramolecular charge transfer between TTF and quinoline molecules.

3. Benchmarking the DFT methods with DLPNO-CCSD(T)-based wave function calculations

We have also carried out the DLPNO-CCSD(T) calculations based on closed-shell the singlet B3LYP-D3/6-31G* geometries of $^*\text{N}_2^0$ and $^*\text{N}_2\text{H}^{+1}$ species, as in Extended Data Fig. 9 and Extended Data Table 8. Such DLPNO-CCSD(T) or DLPNONEVPT2

computations⁴⁴ have been carried out in benchmarking DFT study of N₂ or CO₂ coupling reduction^{45,46}. The high-level single point energy computations using wave function methods were carried out at two basis set levels, including **level5** (def2-TZVP basis set) and **level6** (def2-TZVPP basis set). As shown in Extended Data Table 8, the DFT (B3LYP-D3) predicted relative energy of *N₂H⁺¹ species, $\Delta E=3.96$ eV (**level6**) is in qualitative agreement with that predicted by DLPNO-CCSD(T). In addition, we employed Cluster-in-molecule (CIM)^{47,48}, which is a linear-scaling local correlation method for electron correlation calculations of large systems and combined with the domain based local pair natural orbital (DLPNO) method for coupled cluster calculations of large systems⁴⁹. Here, we performed CIM-DLPNO-CCSD(T) calculations using LSQC 2.4 package⁵⁰ (with an interface to ORCA⁵¹) for the singlet states of *N₂⁰ and *N₂H⁺¹ species (Extended Data Fig. 9), with the results shown in Extended Data Table 8. The B3LYP-D3/def2-TZVP results show small deviations with respect to CIM-DLPNO-CCSD(T)/def2-TZVP results. This implies that the obtained DFT results of the intermediates along the possible reaction pathways are reasonable.

4. Optimized Geometry of intermediates with different functionals

The optimized structures were shown in Extended Data Fig. 8, respectively. The predicted N-N distances (d_{N-N}) in the studied intermediates are insensitive to the choice of different theoretical levels. The difference of the average distance between Zn and N atoms (\bar{d}_{Zn-N}) in the optimized structures by using different levels are no more than 0.16 Å, which is obtained from

$$\bar{d}_{Zn-N} = \frac{1}{n} \sum_{i=1}^n d_{Zn-N_i}$$

where n is the number of the coordination distance between Zn and N atoms, d_{Zn-N_i} is the distance between Zn and N_{*i*} atom, respectively.

5. Spin preference of intermediates calculated by B3LYP-D3

As shown in Extended Data Table 7, the energies of intermediates with different spin states were calculated by B3LYP-D3 with different basis sets (**level1-level4**). The geometrical structures of low-spin and high-spin states were shown in Extended Data Fig. 10. The low-spin states have lower relative energies than the high-spin states along the reaction path of the endothermic process. Thus, we mainly investigated the low-spin states in the nitrogen reduction reaction pathways.

Photocatalytic NRR measurements

The nitrogen fixation tests were conducted in a 250 mL cylindrical quartz reactor with a diameter of 5.0 cm at ambient pressure using a 300 W Xe lamp (350-780 nm; without cutoff filter; illumination area: 19.6 cm²) as the light source. The reactor was cooled with constant water circulation to ensure that the reaction proceeded at 25 °C. Briefly, 20 mg of photocatalyst was uniformly dispersed into 60 mL of deionized water with sonication and then transferred into the reactor. The reactor was bubbled with designated feeding gas flow for 60 min in the dark to obtain a gas-saturated mixture. The ammonia synthesis process was conducted with continuous stirring and

feeding gas bubbling for 180 min under constant Xe lamp illumination. For every 30 min, 3 mL of the solution was removed from the reactor and centrifuged at 10,000 rpm for 10 min to completely remove the photocatalysts. The ammonia concentration was measured using the ion chromatography method (Dionex ICS-900), and the concentration of ammonia was determined from a standard curve using various concentrations of NH₄Cl (0, 8, 16, 48, 80, and 112 μmol/L), as shown in Extended Data Fig. 11.

¹H NMR spectral analysis for ¹⁵N isotope labelling NRR experiments

The isotope labelling experiments were carried out with 20 mg of NJUZ-1 photocatalyst under ¹⁵N₂ atmosphere (¹⁵N₂ 98% enrichment, Sigma) in 40 mL of deionized water. The 98% ¹⁵N₂ gas was purified through 0.05 M HCl in advance (Extended Data Fig. 12a) before flowing into the NNR reactor to exclude the contamination of ammonia impurity that may influence the results of isotope labelling. There is no ammonia contamination as verified by the ¹H NMR spectra in Extended Data Fig. 12b. 6 mL of the suspension was removed from the photocatalytic reactor, centrifuged at 10,000 rpm and acidified with 0.05 M of diluted HCl. The acidified liquid was concentrated to a volume of 1.0 mL through a vacuum-drying process. D₂O was added to a closed tube for ¹H NMR measurements that were performed by a superconducting Fourier transform NMR spectrometer (Bruker Avance-600).

Data availability

The data that support the findings of this study are available from the corresponding authors on reasonable request.

33. Y. Mitamura, H. Yorimitsu, K. Oshima, A. Osuka, Straightforward access to aryl-substituted tetrathiafulvalenes by palladium-catalysed direct C–H arylation and their photophysical and electrochemical properties. *Chem. Sci.* **2**, 2017-2021 (2011).
34. F. Gao, F.-F. Zhu, X.-Y. Wang, Y. Xu, X.-P. Wang, J.-L. Zuo, Stabilizing radical cation and dication of a tetrathiafulvalene derivative by a weakly coordinating anion. *Inorg. Chem.* **53**, 5321-5327 (2014).
35. M. D. Segall, P. J. D. Lindan, M. J. Probert, C. J. Pickard, P. J. Hasnip, S. J. Clark, M. C. Payne, First-principles simulation: ideas, illustrations and the CASTEP code. *J. Phys. Condens. Matter.* **14**, 2717-2744 (2002).
36. J. P. Perdew, K. Burke, M. Ernzerhof, Generalized gradient approximation made simple. *Phys. Rev. Lett.* **77**, 3865-3868 (1996).
37. S. Grimme, J. Antony, S. Ehrlich, H. Krieg, A consistent and accurate ab initio parametrization of density functional dispersion correction (DFT-D) for the 94 elements H-Pu. *J. Chem. Phys.* **132**, 154104 (2010).
38. S. Grimme, S. Ehrlich, L. Goerigk, Effect of the damping function in dispersion corrected density functional theory. *J. Comput. Chem.* **32**, 1456-1465 (2011).
39. J. K. Nørskov, J. Rossmeisl, A. Logadottir, L. Lindqvist, J. R. Kitchin, T. Bligaard, H. Jónsson, Origin of the overpotential for oxygen reduction at a fuel-cell cathode.

- J. Phys. Chem. B.* **108**, 17886-17892 (2004).
40. M. J. Frisch, G. W. Trucks, H. B. Schlegel, J. B. Foresman, D. J. Fox *et al.* *Gaussian 16*, revision **A.03**; Gaussian Inc.: Wallingford, CT, 2016 .
 41. A. Schafer, H. Horn, R. Ahlrichs. Fully optimized contracted Gaussian basis sets for atoms Li to Kr. *J. Chem. Phys.* **97**, 2571-2577 (1992).
 42. J. Tomasi, B. Mennucci, R. Cammi. Quantum Mechanical Continuum Solvation Models. *Chem. Rev.* **105**, 2999-3094 (2005).
 43. A. D. Becke. Density-functional exchange-energy approximation with correct asymptotic behavior. *Phys. Rev. A*, **38**, 3098-3100 (1998).
 44. Z. Ni, Y. Guo, F. Neese, W. Li, S. Li. Cluster-in-Molecule Local Correlation Method with an Accurate Distant Pair Correction for Large Systems. *J. Chem. Theory Comput.* **17**, 756-766 (2021).
 45. Y. Zhao, D. G. Truhlar. A new local density functional for main-group thermochemistry, transition metalbonding, thermochemical kinetics, and noncovalent interactions. *J. Chem. Phys.* **125**, 194101 (2006).
 46. F. Weigend, R. Ahlrichs. Balanced basis sets of split valence, triple zeta valence and quadruple zeta valence quality for H to Rn: Design and assessment of accuracy. *Phys. Chem. Chem. Phys.* **7**, 3297-3305 (2005).
 47. Y. Guo, U. Becker, F. Neese. Comparison and combination of “direct” and fragment based local correlation methods: Cluster in molecules and domain based local pair natural orbital perturbation and coupled cluster theories. *J. Chem. Phys.*, **148**, 124117 (2018).
 48. L. Roy, M. H. Al-Afyouni, D. E. DeRossa, B. Mondal, I. M. DiMucci, K. M. Lancaster, J. Shearer, E. Bill, W. W. Brennessel, F. Neese, S. Ye, Pa. L. Holland. Reduction of CO₂ by a masked two-coordinate cobalt(I) complex and characterization of a proposed oxodicobalt(II) intermediate. *Chem. Sci.*, **10**, 918-929 (2019).
 49. M. Légaré, M. Rang, G. Bélanger-Chabot, J. I. Schweizer, I. Krummenacher, R. Bertermann, M. Arrowsmith, M. C. Holthausen, H. Braunschweig. The reductive coupling of dinitrogen. *Science*, **363**, 1329-1332 (2019).
 50. S. Li, J. Ma, Y. Jiang. Linear scaling local correlation approach for solving the coupled cluster equations of large systems. *J. Comput. Chem.*, **23**, 237-244 (2002).
 51. F. Neese, F. Wennmohs, U. Becker, Christoph Riplinger. The ORCA quantum chemistry program package. *J. Chem. Phys.*, **152**, 224108 (2020).

Acknowledgments This work was supported by the National Basic Research Program (2018YFA0306004 and 2017YFA0208200), the National Natural Science Foundation of China (22022505, 22033004, 21875099, 21872069 and 21631006), the Fundamental Research Funds for the Central Universities of China (0205-14380219, 0205-14913212), the Natural Science Foundation of Jiangsu Province (BK20180008), and the High-Level Innovation and Entrepreneurship Project of Jiangsu Province of China.

Author contributions J.-L.Z, Z.J., Y.X. and B.L. conceived the idea of this study and designed the experiments. B.L. performed the sample synthesis. Y.X. and B.L. performed photoelectric measurements, catalytic tests and data analysis. Y.M.G., Z.G.N., S.H.L. and J.M. performed theoretical calculations. Y.X. and B.L. performed the material characterizations. All the authors analyzed the data and discussed the results. Y.X., B.L., T.Y., J.M. Z.J. and Z.-J.L. co-wrote and revised the manuscript. Z.J. and Z.-J.L. supervised the project.

Competing financial interests The authors declare no competing interests.